



Highly efficient photocatalytic removal of sodium pentachlorophenate with Bi₃O₄Br under visible light

Jiling Wang, Ying Yu, Lizhi Zhang*

Key Laboratory of Pesticide & Chemical Biology of Ministry of Education, Institute of Environmental Chemistry, College of Chemistry, Central China Normal University, Wuhan 430079, PR China



ARTICLE INFO

Article history:

Received 1 December 2012

Received in revised form 27 January 2013

Accepted 3 February 2013

Available online 10 February 2013

Keywords:

Bismuth oxybromide

Visible light

Photocatalysis

Sodium pentachlorophenate

Degradation

ABSTRACT

In this study we demonstrate that Bi₃O₄Br is a superior visible light driven photocatalyst for the decomposition and mineralization of a typical chlorinated phenol derivative sodium pentachlorophenate. It could remove more than 92% of sodium pentachlorophenate with concentration of 40 mg/L under visible light irradiation from 500 W Xe-lamp with a 420 nm cut off filter in 15 min, accompanying with 80% of mineralization. Density functional theory (DFT) calculation and systematical characterization reveal that high efficient visible light driven sodium pentachlorophenate removal with Bi₃O₄Br could be attributed to effective separation and transfer of photoinduced charge carriers in Bi₃O₄Br with narrower band gap and more negative conduction band position, which favors the photogenerated electrons trapping with molecular oxygen to produce •O₂⁻. The •O₂⁻ radicals could not only inhibit the recombination of photoinduced charge carriers, but also benefit the dechlorination of chlorinated phenol derivative. The visible light induced degradation pathway of sodium pentachlorophenate was carefully investigated with high performance gas chromatography–mass spectrometry. This study provides a new photocatalyst for chlorinated phenol derivative removal with solar light.

© 2013 Elsevier B.V. All rights reserved.

1. Introduction

As a highly chlorinated phenol derivative sodium pentachlorophenate (NaPCP) has been classified as a priority contaminant by the US, European Union and China [1–3]. Many methods have been explored to degrade NaPCP, including photo-Fenton reaction [3,4], biological degradation [5], and photocatalysis [6]. Among these methods photocatalytic removal of NaPCP with semiconductors is very attractive because of its high effectiveness and utilization of solar light. For example, Ji et al. demonstrated that 90% of NaPCP with concentration of 50 mg/L could be removed by NaBiO₃ in 1 h under visible light irradiation ($\lambda > 400$ nm, 500 W Xe lamp) [7]. Wang and co-workers reported that the degradation of NaPCP with concentration of 20 mg/L over V-N co-doped TiO₂ nanoparticles under visible light ($\lambda > 400$ nm, 400 W Xe lamp) could be finished in 2 h [8].

Bismuth oxyhalides BiOX (X=Cl, Br, I) belong to a new family of visible light driven photocatalysts and attract more and more attention because of their interesting structure dependent photocatalytic performance arisen from their layered structure interleaved with [Bi₂O₂] slabs and double halogen atoms slabs [9–11]. The layered structure could not only benefit the separation

of photogenerated charge carriers under the influence of internal electric fields between the [Bi₂O₂] and halogen layers [12,13], but also reduce surface trapping of photogenerated carriers because surface defects might be controlled to as few as possible owing to the low dangling bond arisen from covalent bond nature of the layers. Among these bismuth oxyhalides, BiOBr has attracted increasing interest because of its desirable band gap of about 2.7 eV for visible light photocatalysis [9]. For example, our group recently reported hierarchical BiOBr nanoplate microspheres could effectively remove NO in indoor air under visible light irradiation [14,15]. Tang's group used the self-assembled BiOBr nanoflake to degrade methyl orange under visible light [16]. However, the photocatalytic performance of BiOBr is still not satisfactory for potential application. Therefore, many scientists seek for effective methods to improve the photocatalytic activity of BiOBr. For instance, Wang and co-workers found that iodine doping could enhance the visible light absorption and photocatalytic activity of 3D BiOBr microspheres via the band gap narrowing owing to the formation of BiOBr_xI_{1-x} solid solution photocatalyst [12]. Our group demonstrated that BiOBr-graphene nanocomposites exhibited greatly enhanced visible light driven NO removal efficiency in comparison with BiOBr because the presence of graphene could facilitate the separation of photo-induced electron–hole pairs [15]. However, there is no report of chlorinated phenol derivative photodegradation with bismuth oxybromide photocatalysts, which might be owing to their low efficiencies on chlorinated

* Corresponding author. Tel.: +86 27 6786 7535; fax: +86 27 6786 7535.

E-mail address: zhangl@mail.ccnu.edu.cn (L. Zhang).

phenol removal. For the purpose of high efficient chlorinated phenol derivative removal with utilization of solar energy, we are still required to design and develop more visible light active bismuth oxybromide based photocatalysts.

In this study we first evaluate the photocatalytic NaPCP removal performance with BiOBr under visible light irradiation. Through theoretical calculation we attribute the undesirable photocatalytic performance of BiOBr to its too positive conduction band. As increasing Bi content in bismuth containing photocatalysts could shift the conduction band negatively, we therefore propose that $\text{Bi}_3\text{O}_4\text{Br}$ might exhibit better photocatalytic performance than BiOBr. On the basis of these analyses, we selectively prepare BiOBr and $\text{Bi}_3\text{O}_4\text{Br}$ nanoflakes with a facile pH controlled hydrothermal method and compare their performances to remove toxic organic pollutant sodium pentachlorophenate under visible light. The photocatalysis mechanism and the enhanced visible light photocatalytic activity of $\text{Bi}_3\text{O}_4\text{Br}$ are investigated in detail. The degradation pathway of sodium pentachlorophenate is also studied carefully.

2. Experimental

2.1. Theoretical calculation

The quantum-mechanical calculations were carried out using the density functional theory (DFT). Exchange-correlation effects were considered by using of generalized gradient approximation (GGA). The total energy was tested by CASTEP according pseudopotentials to describe electron-ion interactions and represent electronic wave. The cut off of kinetic energy was set at 340 eV [17,18].

2.2. Preparation of BiOBr and $\text{Bi}_3\text{O}_4\text{Br}$

The nanoflakes of BiOBr and $\text{Bi}_3\text{O}_4\text{Br}$ were directly prepared by hydrothermal method. All chemicals were purchased from Sinopharm Chemical Reagent Co., Ltd. (Shanghai, China) without further purification. For the preparation of $\text{Bi}_3\text{O}_4\text{Br}$, 1.0 g of $\text{Bi}(\text{NO}_3)_3 \cdot 5\text{H}_2\text{O}$ and 1.0 g of hexadecyltrimethylammonium bromide (CTAB) were dissolved in 50 mL of deionized water for stirring 10 min. Then 1 mol/L NaOH aqueous solution was added dropwise to adjust the pH value of the solution to 11.5. The resulting solution were stirred for 1 h at room temperature and then transferred into 100 mL autoclave filled up to 75% of the total volume. The resulting mixtures were heated at 160 °C for 18 h. Finally, the resulting precipitate was collected, washed thoroughly with deionized water and ethanol several times, and dried at 50 °C in air. For comparison, BiOBr was obtained by using the same procedure without adding NaOH.

2.3. Characterizations

X-ray diffraction (XRD) of as-prepared samples was characterized on a Rigaku Ultima III X-ray diffractometer using Cu K α radiation ($\lambda = 0.15418 \text{ nm}$). The morphologies and particle size of the samples were further investigated by scanning electron microscopy (SEM, JEOL 6700-F) and transmission electron microscopy (TEM, JEOL JSM-2010). Diffuse reflectance spectra (DRS) were conducted on a Hitachi U-3010 UV-vis spectrophotometer. Nitrogen adsorption-desorption isotherms were collected on a Micromeritics Tristar-2000 surface area and porosity analyzer at 77 K after the sample had been degassed in the flow of N_2 at 180 °C for 5 h. Surface electronic states were analyzed by X-ray photoelectron spectroscopy (XPS, VG Multilab 2000). The charge effect was calibrated by using the binding energy of C 1s peak at 284.6 eV.

2.4. Photocatalytic degradation of NaPCP

The photocatalytic activities of the BiOBr and $\text{Bi}_3\text{O}_4\text{Br}$ were evaluated by degradation of NaPCP (40 mg/L) under 500 W Xe-lamp with a 420 nm cut off filter. All experiments processed at room temperature to avoid any thermal catalytic effect by using the circulating water jack. During the reaction, 50 mg of the catalyst was suspended into 50 mL of aqueous solution which contains pollutant. Before irradiation the solution was magnetically stirred for 1 h in the dark to ensure the establishment of an adsorption-desorption equilibrium of pollutants on catalyst surface. At irradiation time interval of 5 min, 3 mL of solutions were collected and then centrifuged and filtered through a 0.22 μm membrane filter for analysis.

2.5. Analytical methods

The concentration of NaPCP was recorded by using a high-performance liquid chromatography (HPLC, Shimadzu LC-20A, Japan). The measuring conditions were TC-C18 reverse phase column, injection volume of 10 μL , 0.15% of acetic acid/methanol = 20:80, column temperature of 30 °C, flow rate of 0.8 mL/min and detection wavelength of 254 nm. The intermediates generated in the photocatalytic process were detected by high performance gas chromatography-mass spectrometry (GC-MS, Agilent 6890N-5973). Before the analysis, 2 mL of dichloromethane (Alfa Aesar) was used to extract 1 mL of sample. The column temperature was 50 °C for 3 min, then increased to 200 °C with a rate of 10 °C/min, and maintained at 200 °C for 10 min. Later the column temperature was raised to 270 °C with a rate of 20 °C/min, and kept at 270 °C for 5 min. The injected sample was retained at 260 °C after injection. Hydrogen peroxide concentrations were determined by using the fluorescence method [19]. Electron spin resonance (ESR) spectra with 5,5-dimethyl-1-pyrroline-N-oxide (DMPO) as the radical spin-trapped reagent were determined on a Bruker ESR 300E spectrometer [20,21]. The concentration of DMPO was 0.2 mol/L, and the irradiation source was a 500 W Xe lamp with a cut off filter ($\lambda > 420 \text{ nm}$). Total organic carbon (TOC) content in water was determined by a Shimadzu TOC-V CPH analyzer.

2.6. Electrochemical measurements

For the preparation of photoanode, 50 mg of sample, 200 μL of distilled water and 40 μL of PEDOT-PSS conductive solution with 2.2–2.6% of poly (3,4-ethylenedioxythiophene)-poly(styrenesulfonate) in water were mixed and then grinded for about 10 min. The resulted paste was then spread on a fluorine-doped tin oxide (FTO) conducting glass and allowed to dry under the 160 °C for 10 min. Electrochemical measurements were taken by using an electrochemical analyzer (CHI660D, CHI Shanghai, Inc.) in a standard three electrode system with a platinum plate as the counter electrode, the prepared photoanode ($0.5 \times 3 \text{ cm}^2$) as the working electrode, and saturated calomel electrode (SCE) as the reference electrode, which immersed in a 50 mL glass breaker contained 0.5 M Na_2SO_4 aqueous solution as the electrolyte, respectively. Time dependent photocurrent curves were measured with amperometric $i-t$ curve method. The Mott-Schottky experiments were carried out with independence-potential model to evaluate the band positions of the catalysts.

3. Results and discussion

In this study, we first tested the performance of BiOBr on the degradation of NaPCP under visible light and found BiOBr could only remove 10% of NaPCP with concentration of 40 mg/L under visible light irradiation from 500 W Xe-lamp with a 420 nm cut

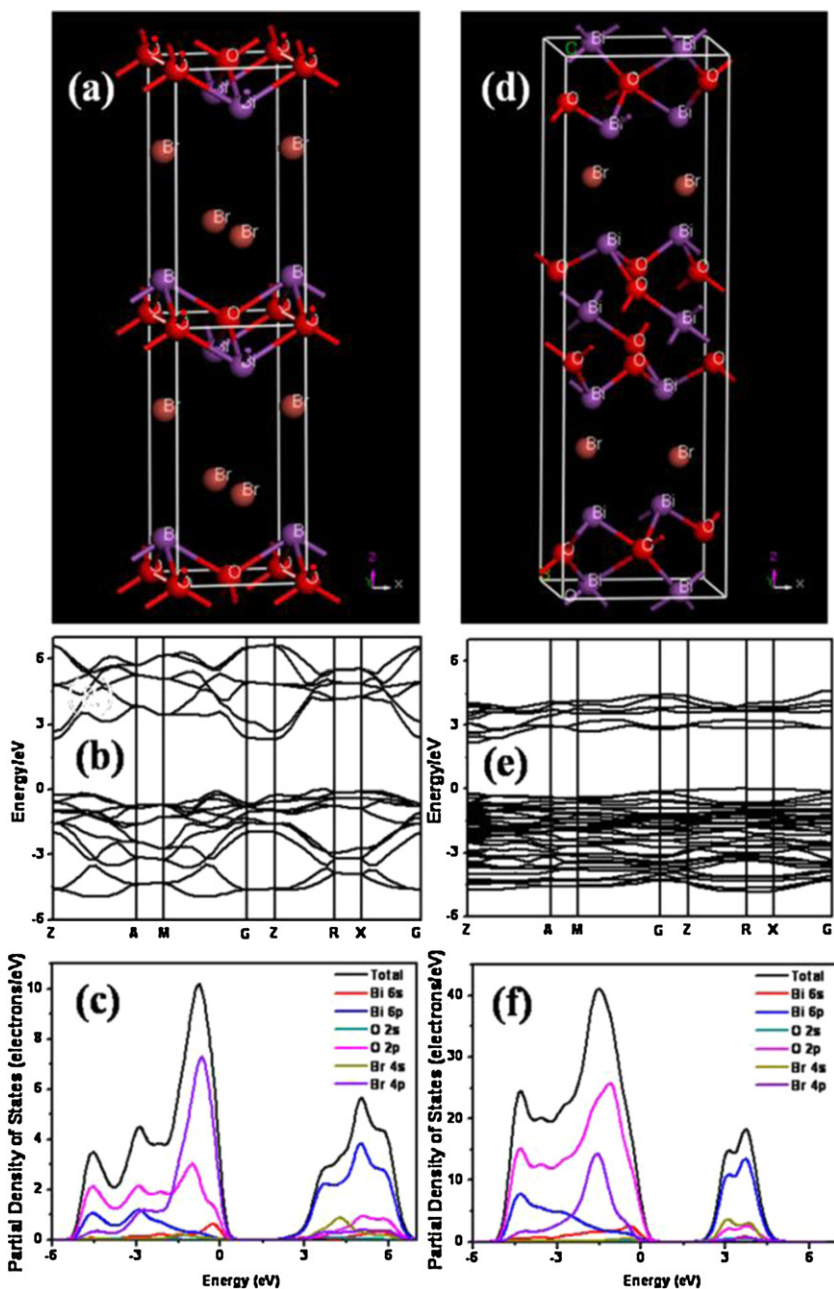


Fig. 1. The crystal structure of BiOBr and Bi₃O₄Br (a, d); calculated band structures of BiOBr and Bi₃O₄Br (b, e); and PDOS of BiOBr and Bi₃O₄Br obtained by GGA (c, f).

off filter in 15 min. Obviously, this photocatalytic performance might not be desirable for potential application. To find out the intrinsic reasons for the undesirable photocatalytic performance of BiOBr, we calculated the band structure of BiOBr by the plane-wave density function theory (DFT) with using the CASTEP package. The crystal structure reveals that BiOBr contains a bilayer structure of [Bi₂O₂] and [Br] slabs, which construct tetragonal BiOBr along the c axis (Fig. 1a). The electronic band structure displays an indirect semiconductor nature of BiOBr, beneficial for the separation of photogenerated charge carriers (Fig. 1b). The conduction band bottom of BiOBr is generally made up of Bi 6p orbital and a certain extent of O 2p and Br 4p orbital. It is known that the conduction band of BiOBr was too positive for molecular oxygen to trap photogenerated electrons to produce •O₂⁻, resulting in fast recombination of photogenerated charge carriers and less generation of reactive oxygen species [22,23]. However, the generation of •O₂⁻ is an important process during photocatalysis. The

•O₂⁻ radicals could not only inhibit the recombination of photoinduced charge carriers, but also benefit the dechlorination of chlorinated phenol derivative, which favor the subsequent broken of benzene ring of chlorinated phenol derivatives [24]. On the basis of the above theoretical analysis, we conclude that the lower photocatalytic performance of BiOBr might be attributed to its undesirable positions of conduction bands although BiOBr possesses promising characteristics such as layered structure, indirect semiconductor and suitable band gap of about 2.7 eV for visible light photocatalysis. Therefore, it would be a right way to develop highly visible light active photocatalysts with more negative conduction band position than that of BiOBr, but reserving layered structure and band gap suitable for visible light harvest. Obviously, this objective could not be achieved via metal or non-metal doping in BiOBr because the resulting doped photocatalysts often suffer from thermal instability and other shortcomings arisen from the doping elements which could serve as the recombination centers for

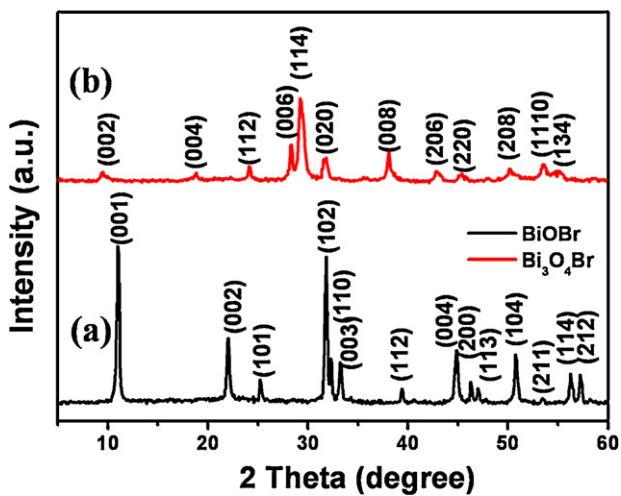


Fig. 2. XRD patterns of (a) BiOBr and (b) Bi₃O₄Br.

the photogenerated carriers. Some alternative strategies are thus required.

It was recently reported that increasing Bi content in bismuth containing photocatalysts could shift the conduction band negatively and thus significantly enhance photocatalytic performance [25]. It is therefore reasonable to assume Bi₃O₄Br might exhibit better photocatalytic performance than BiOBr because Bi₃O₄Br is a layered structure indirect semiconductor with suitable band gap and more Bi content than BiOBr. To verify this assumption, we also calculated the band structure of Bi₃O₄Br by the plane-wave density function theory (DFT) with using the CASTEP package. DFT calculations reveal that the interconnection of Bi atoms and O atoms in Bi₃O₄Br is different from that of BiOBr. In BiOBr each Bi atom coordinates by four O atoms and four Br atoms, while the Bi atoms in Bi₃O₄Br have two coordination environments including coordination with three O atoms and two Br atoms and connection with four O atoms. The Bi and O atoms are connected by bond interactions to form [Bi₃O₄] layers, which then stack with Br atoms with van

der Waals interaction to produce layered orthorhombic Bi₃O₄Br (Fig. 1d). The partial density of states (PDOS) analysis reveals that the two bismuth oxybromides possess similar composition of band structure but different intensity of Bi 6p orbital in CB (Fig. 1c and f). The theoretical band gap of BiOBr and Bi₃O₄Br were calculated to be 2.31 and 2.17 eV, respectively. The intensity of Bi 6p orbital in CB bottom of Bi₃O₄Br is stronger than that of BiOBr, suggesting a more negative conduction band.

The above theoretical calculation results encourage us to seek for a facile method to prepare Bi₃O₄Br for efficient photocatalytic removal of NaPCP. Literature search revealed that Li and his co-workers previously reported a pH controlled hydrothermal route to synthesize various Bi_xO_yBr_z [26,27]. During their synthesis, BiOBr was formed at the beginning of the reaction. With adding NaOH, Br⁻ gradually was substituted by OH⁻, resulting in the formation of bismuth oxybromide with high Bi content. We therefore employed Li's strategy to selectively prepare Bi₃O₄Br and BiOBr by controlling the pH values during the synthesis. X-ray diffraction (XRD) analysis (Fig. 2) reveals the as-prepared samples are tetragonal phase BiOBr (JCPDS card No. 3-733) and orthorhombic Bi₃O₄Br (JCPDS card No. 84-793) synthesized in the absence or presence of NaOH, respectively. The sharp diffraction peaks and no impurity peaks indicate their highly crystalline nature and high purity, respectively. SEM was further used to investigate the morphologies of the two samples (Fig. 3). Both BiOBr and Bi₃O₄Br samples consist of plenty of irregular plates. The plates of BiOBr are 0.7–2.0 μm in width and 50 nm in thickness. The width of Bi₃O₄Br plates is 0.3–1.5 μm in size, smaller than that of BiOBr, while the thickness is 20–40 nm, thinner than that of BiOBr. The nanoplate structures of BiOBr and Bi₃O₄Br were further confirmed by TEM and HRTEM (Fig. 3). The HRTEM images also confirm the high crystalline nature of the samples. The clear lattice fringes with an interplaner lattice spacing of 0.28 nm is in accordance with the (110) plane of tetragonal BiOBr. While the adjacent lattice planes of 0.20 nm could be indexed to the (220) plane of Bi₃O₄Br. Moreover, the selected area electron diffraction (SAED) patterns of nanoplates exhibit a regular and clear square diffraction spot array, revealing the single-crystal nature of BiOBr and Bi₃O₄Br. The fast Fourier transform (FFT) patterns of the yellow and red square

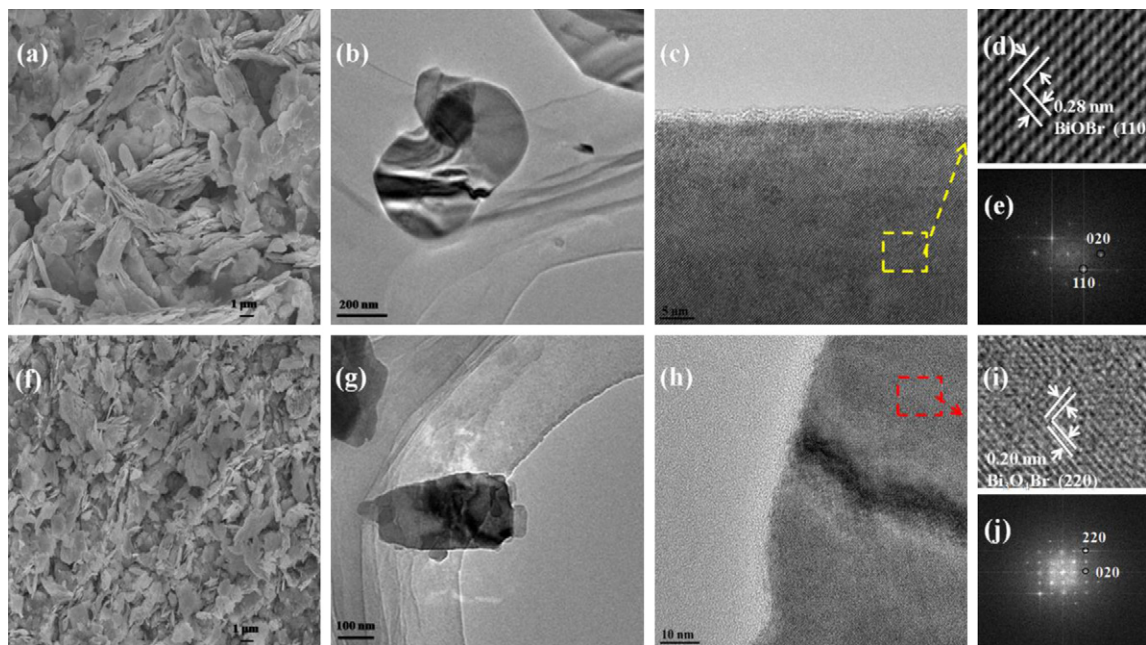


Fig. 3. SEM images of (a) BiOBr and (f) Bi₃O₄Br; (b) TEM images; (c, d) HRTEM images; and (e) FFT patterns of BiOBr; (g) TEM images; (h, i) HRTEM images; and (j) FFT patterns of Bi₃O₄Br.

Table 1

Summary of physicochemical properties and photocatalytic activities of P25, BiOBr and Bi₃O₄Br.

Samples	$A_{\text{BET}}^{\text{a}}$ ($\text{m}^2 \text{g}^{-1}$)	Band gap ^b (eV)	$f_{\text{NaPCP}}^{\text{c}}$ (%)	$k_{\text{NaPCP}}^{\text{d}}$ ($\times 10^{-3} \text{ min}^{-1}$)	$k'_{\text{NaPCP}}^{\text{e}}$ ($\text{g min}^{-1} \text{ m}^{-2}, \times 10^{-3}$)
BiOBr	4.1	2.7	10.1	7.36	1.78
Bi ₃ O ₄ Br	8.5	2.4	92.3	168	19.8
P25	50	3.2	3.8	1.81	0.036

^a The specific surface area.

^b The band gap energy.

^c The removal efficiency of NaPCP on photocatalysts after 15 min.

^d The ratio of degradation NaPCP over photocatalysts.

^e The k' values were k values normalized with the surface area.

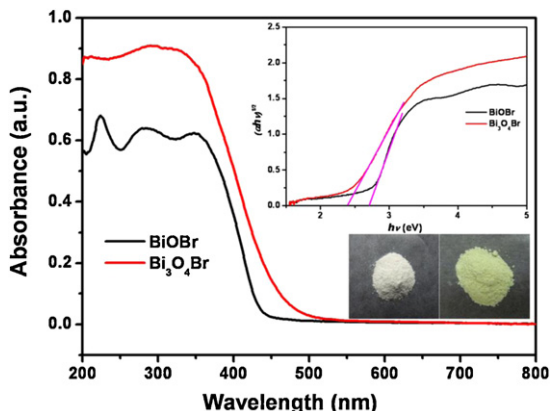


Fig. 4. UV-vis diffuse reflectance spectra and plots of $(\alpha h\nu)^{1/2}$ versus energy ($h\nu$) for the band gap energies BiOBr and Bi₃O₄Br.

regions reveal that both BiOBr and Bi₃O₄Br expose with (0 0 1) crystal planes. The surface areas of BiOBr and Bi₃O₄Br are 4.1 and 8.5 m^2/g (Table 1), respectively. The higher surface area of Bi₃O₄Br should be attributed to its smaller size of nanoplates.

The as-prepared BiOBr and Bi₃O₄Br are respectively light yellow and kelly in appearance (Fig. 4), suggesting they possess different intrinsic optical properties. Further UV-vis diffuse reflectance spectra (DRS) analysis reveals that BiOBr and Bi₃O₄Br have an absorption edge up to about 430 and 467 nm, respectively. It is known that the optical absorption of semiconductor near the band edge follows the formula $\alpha h\nu = A(h\nu - E_g)^{n/2}$, where α , ν , E_g , and A are the absorption coefficient, light frequency, band-gap energy, and a constant, respectively. While n is a constant that depends on the characteristics of the transition in the semiconductor, namely, direct transition ($n = 1$) or indirect transition ($n = 4$). Therefore, the band-gap energy (E_g value) of the products could be estimated from a plot $(\alpha h\nu)^{1/2}$ versus photon energy ($h\nu$). The values of band gap energy of BiOBr were respectively estimated to be 2.7 and 2.4 eV for Bi₃O₄Br (Table 1), higher than the calculated values. The smaller

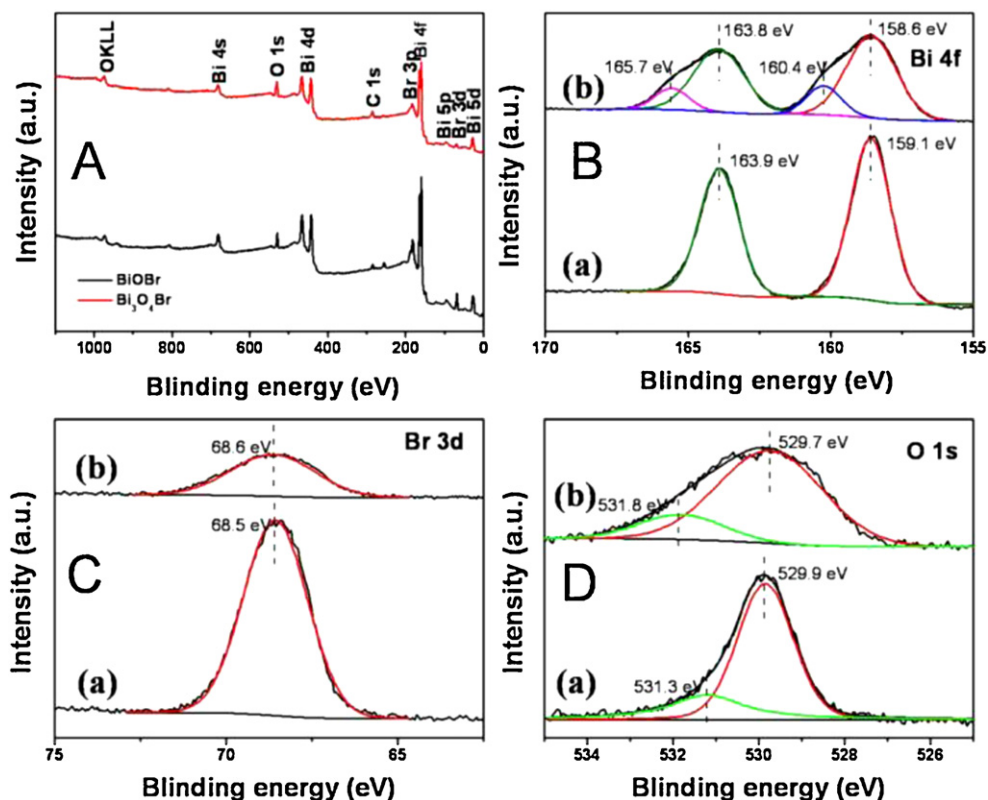


Fig. 5. XPS survey spectrum of BiOBr and Bi₃O₄Br samples (A). The high-resolution XPS spectra of (a) BiOBr and (b) Bi₃O₄Br samples in the regions of Bi 4f (B), Br 3d (C), and O 1s (D).

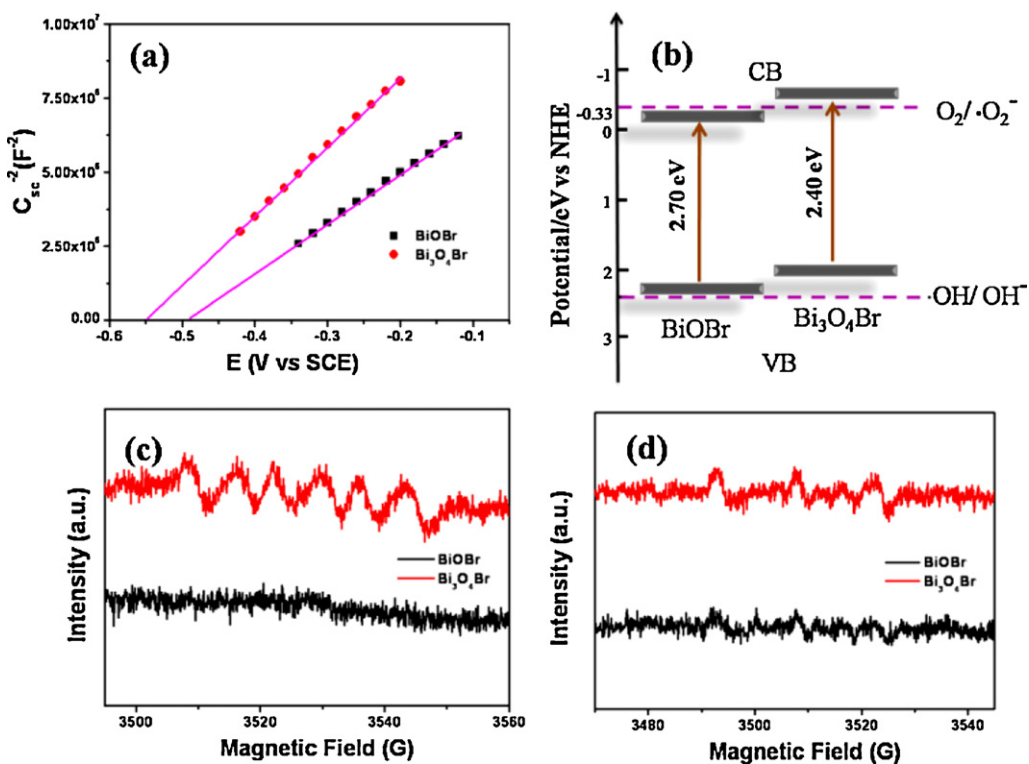


Fig. 6. (a) Mott-Schottky plots for the BiOBr and Bi₃O₄Br electrodes; (b) estimated band positions of BiOBr and Bi₃O₄Br as well as the reduction potentials of O₂/·O₂⁻ and ·OH/OH⁻; (c) DMPO spin-trapping ESR spectra of BiOBr and Bi₃O₄Br methanol dispersion for DMPO-·O₂⁻; (d) DMPO spin-trapping ESR spectra of BiOBr and Bi₃O₄Br in aqueous dispersion for DMPO-·OH.

band gap of Bi₃O₄Br might be arisen from strongly hybridization of O 2p and Bi 6p.

The chemical composition and surface chemical states of BiOBr and Bi₃O₄Br was further studied by X-ray photoelectron spectroscopy (Fig. 5). Both BiOBr and Bi₃O₄Br catalysts consist of the Bi, O and Br elements without existence of other impurity element. Two symmetric peaks at 159.1 and 163.9 eV in the high-resolution Bi 4f of BiOBr are attributed to Bi 4f_{7/2} and Bi 4f_{5/2}, which the charge population is +1.37 for Bi in BiOBr. As for Bi₃O₄Br, Bi 4f region can be fitted into four peaks at 158.6, 160.4, 163.8 and 165.7 eV, respectively. The two charge populations of +1.31 and +1.54 reveal two coordination environments of Bi in Bi₃O₄Br, consistent with the aforementioned theoretical calculation results. The O 1s of BiOBr can be fitted by two peaks at about 529.9 and 531.3 eV, which can

be attributed to lattice oxygen in BiOBr and O—H bonds on the surface, respectively [28]. For O 1s in Bi₃O₄Br, the binding energy can also be fitted with two peaks at about 529.7 and 531.8 eV arisen from lattice oxygen and surface O—H bonds, respectively. Only one symmetric peak at about 68.6 eV was observed for Br 3d of BiOBr and Bi₃O₄Br, indicating their similar coordination of Br.

It is known that the flat band potential of n-type semiconductors could be estimated with Mott-Schottky plots and the bottom of CB of many n-type semiconductors is more negative by ~−0.1 V than the flat band potential [29,30]. The flat band potentials of BiOBr and Bi₃O₄Br are calculated to be about −0.48 V vs SCE (~−0.23 V vs NHE) and −0.55 V vs SCE (~−0.30 V vs NHE), respectively. So the CB of BiOBr and Bi₃O₄Br are estimated to be −0.33 and −0.40 V vs NHE, respectively (Fig. 6a). Since the reduction potential of O₂/·O₂⁻

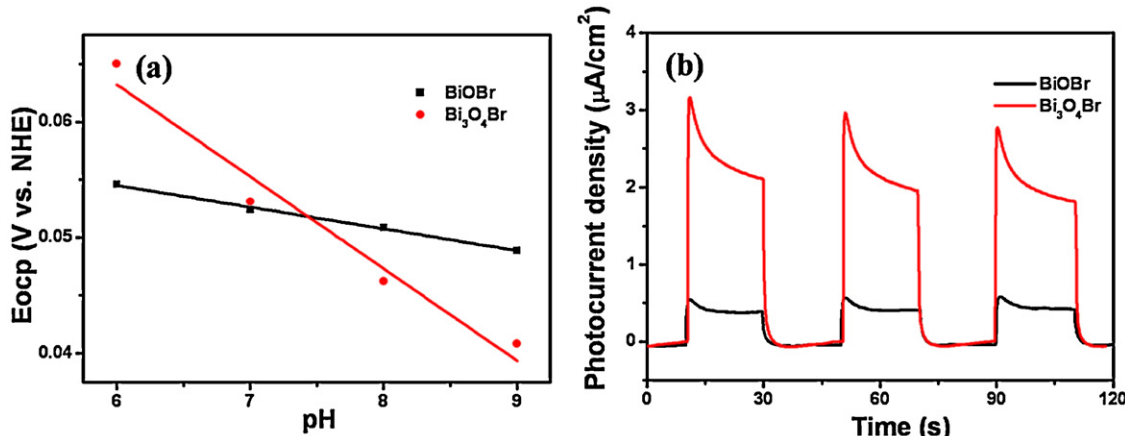


Fig. 7. The open-circuit potentials to the normal hydrogen electrode (a) in electrolyte solution (10 mM KCl). Photocurrent responses of BiOBr and Bi₃O₄Br (b) in 0.5 M Na₂SO₄ aqueous solution under visible light irradiation.

is -0.33 V vs NHE, it is not easy for BiOBr to trap molecular oxygen to generate $\bullet\text{O}_2^-$ under visible light irradiation, but feasible for $\text{Bi}_3\text{O}_4\text{Br}$ because of more negative CB of $\text{Bi}_3\text{O}_4\text{Br}$, agreeing with aforementioned theoretical calculation results. Fig. 6b presents the estimated band positions of BiOBr and $\text{Bi}_3\text{O}_4\text{Br}$ and the reduction potentials of $\text{O}_2/\bullet\text{O}_2^-$ and $\bullet\text{OH}/-\text{OH}$. Meanwhile, ESR spin-trap with DMPO technique was employed to detect reactive oxygen species generated over BiOBr and $\text{Bi}_3\text{O}_4\text{Br}$ under visible light irradiation (Fig. 6c and d). Six characteristic peaks of DMPO- $\bullet\text{O}_2^-$ were only observed in the $\text{Bi}_3\text{O}_4\text{Br}$ methanol suspension under visible light irradiation, not for BiOBr, confirming that the photogenerated electrons on the CB of $\text{Bi}_3\text{O}_4\text{Br}$ could be trapped by molecular oxygen to generate $\bullet\text{O}_2^-$ under visible light. The weak signals of DMPO- $\bullet\text{OH}$ appeared in the $\text{Bi}_3\text{O}_4\text{Br}$ aqueous suspension could be attributed to the generation of $\bullet\text{OH}$ via further reduction of $\bullet\text{O}_2^-$ because both VBs of BiOBr and $\text{Bi}_3\text{O}_4\text{Br}$ could not oxidize surface hydroxyl group or water to generate $\bullet\text{OH}$ (Fig. 6b) [12]. We also utilized the photoluminescence method to detect hydroxyl radical by reacting terephthalic acid with hydroxyl radical to produce highly fluorescent product. No signal was generated from both BiOBr and $\text{Bi}_3\text{O}_4\text{Br}$ suspensions after adding $\text{K}_2\text{Cr}_2\text{O}_7$ to capture the photogenerated electrons, ruling out the generation of $\bullet\text{OH}$ by photogenerated holes.

The photocatalytic performance of semiconductors strongly depend on their photoinduced charge carriers separation and transfer property, which could determine the amounts of photogenerated holes and electrons reaching the surface of photocatalysts. Only these surface-reached photogenerated holes and electrons could react with organic pollutants and/or molecular oxygen. We carefully studied the photoinduced charge transfer properties of BiOBr and $\text{Bi}_3\text{O}_4\text{Br}$. Generally, the semiconductors have the ability to generate electrons and holes upon light irradiation at a suitable energy. Meanwhile, the surface potential

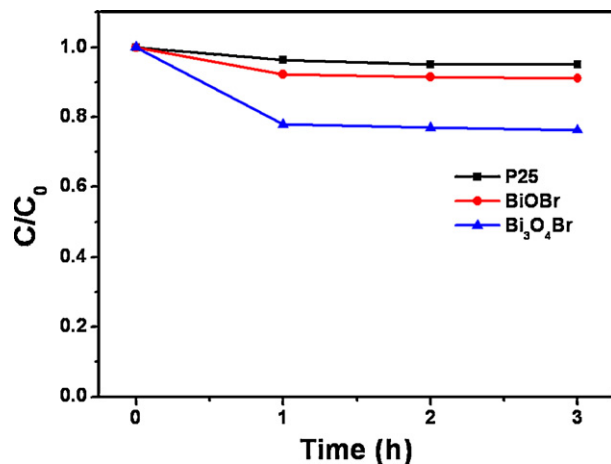


Fig. 8. Time profiles of adsorption of NaPCP over P25, BiOBr and $\text{Bi}_3\text{O}_4\text{Br}$.

gradient reflects the surface-specific charge density accumulation, which can be measured via open-circuit potential change with pH values (E_{ocp}) [31]. A more negative slope of the curve of open-circuit potential versus pH values was observed for $\text{Bi}_3\text{O}_4\text{Br}$, revealing a higher density of charge accumulation over the surface of $\text{Bi}_3\text{O}_4\text{Br}$ and more efficient separation and transfer of the photogenerated electron-hole pairs (Fig. 7a). Meanwhile, a much higher current density of $\text{Bi}_3\text{O}_4\text{Br}$ than that of BiOBr in the current-voltage curves under visible light irradiation demonstrates better effective charge separation and transfer as well as electron collection over $\text{Bi}_3\text{O}_4\text{Br}$ (Fig. 7b), consistent with surface potential gradient measurement. The observed higher current density of $\text{Bi}_3\text{O}_4\text{Br}$

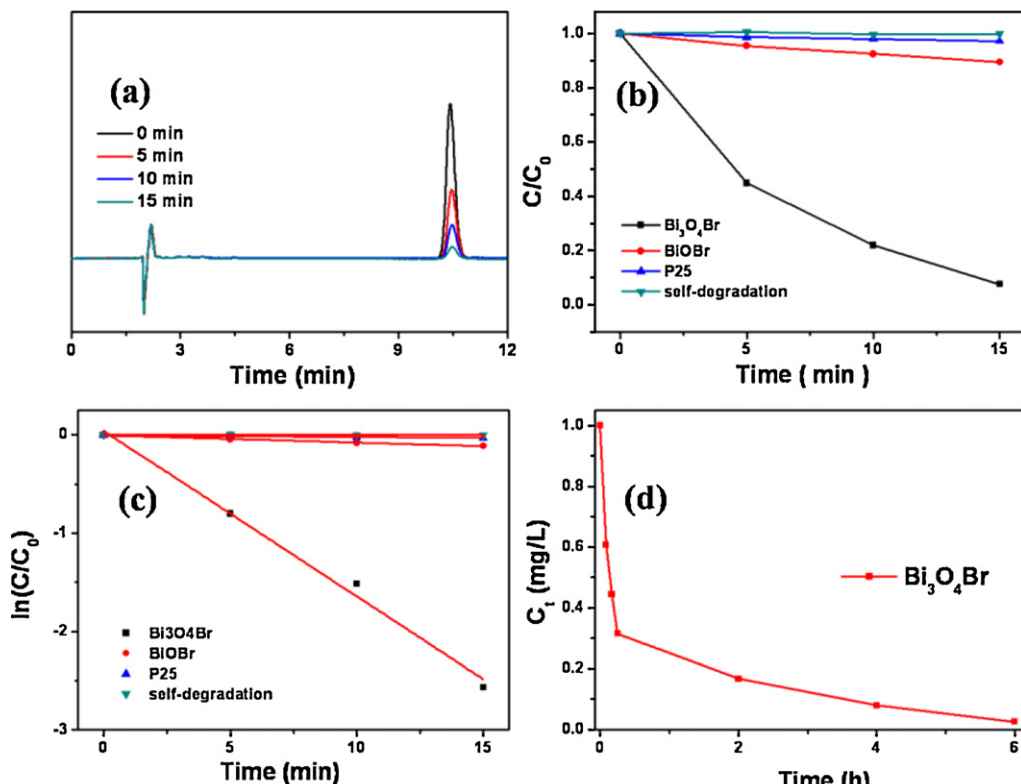


Fig. 9. (a) The HPLC spectra of NaPCP with the various reaction time over $\text{Bi}_3\text{O}_4\text{Br}$ under visible light. (b) Photocatalytic degradation efficiencies of NaPCP over P25, BiOBr, $\text{Bi}_3\text{O}_4\text{Br}$ and self-degradation efficiencies of NaPCP under visible light irradiation. (c) Pseudo first-order kinetics curves of NaPCP degradation in (b). (d) The decrease of TOC during photocatalytic degradation of NaPCP on $\text{Bi}_3\text{O}_4\text{Br}$ under visible light irradiation.

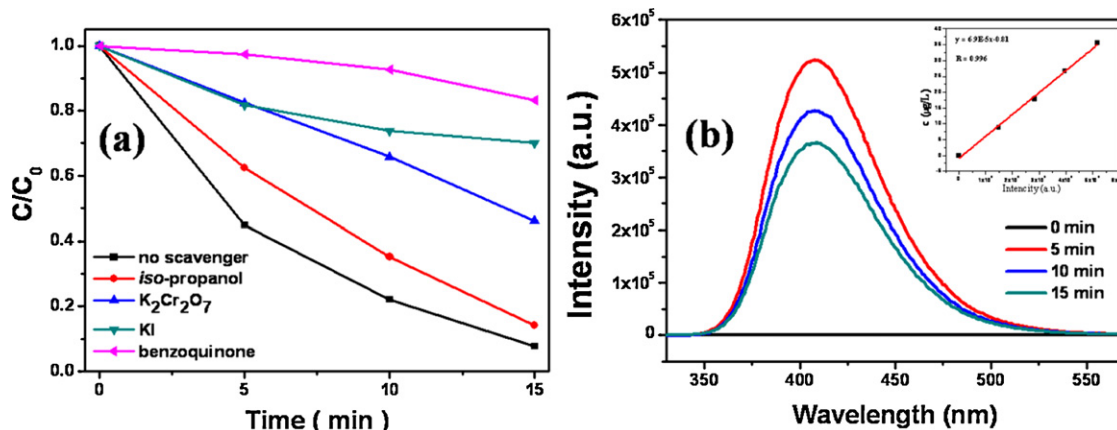


Fig. 10. (a) Photodegradation of NaPCP over Bi_3O_4Br in the presence of different scavengers. (b) The detection of H_2O_2 produced during Bi_3O_4Br photocatalysis.

should be attributed to its narrower band gap and more negative conduction band position.

All the above theoretical and experimental results imply that Bi_3O_4Br would be a superior visible light driven photocatalyst for chlorinated phenol derivative removal. Now it is time for us to assess the real visible light driven photocatalytic performance of Bi_3O_4Br to remove NaPCP to verify our assumption. We used P25 as a standard photocatalyst for comparison. Before the photodegradation process we carefully examined the NaPCP adsorption process over P25, BiOBr and Bi_3O_4Br and found that 5%, 10% and 25% of NaPCP were respectively adsorbed by P25, BiOBr and Bi_3O_4Br (Fig. 8), which should be attributed to their different adsorption capacity. Under visible light irradiation, Bi_3O_4Br could remove more than 92% of NaPCP (Table 1) with concentration of 40 mg/L under visible light irradiation from 500 W Xe-lamp with a 420 nm cut off filter in 15 min, which is much faster than the case (10%) of BiOBr and 3.8% for P25 (Fig. 9b). The variation of HPLC spectra for NaPCP with the reaction time over Bi_3O_4Br under visible light was shown in Fig. 9a. The NaPCP photodegradation process was found to follow pseudo first-order decay kinetics. The NaPCP degradation constant ($1.68 \times 10^{-1} \text{ min}^{-1}$) over Bi_3O_4Br was 22 times that ($7.36 \times 10^{-3} \text{ min}^{-1}$) of BiOBr and 93 times that ($1.81 \times 10^{-3} \text{ min}^{-1}$) of P25 and 617 times that ($2.72 \times 10^{-4} \text{ min}^{-1}$) of self-degradation (Fig. 9c). It is known that surface area of catalysts could influence their photocatalytic performance. To rule out the influence of surface area, we further normalized the NaPCP degradation constants with surface areas and found

the normalized NaPCP degradation constant over Bi_3O_4Br was still 11 times that of BiOBr and 94 times that of P25 (Table 1). Thus the better photocatalytic performance of Bi_3O_4Br is arisen from its intrinsic structure. TOC analysis revealed that 70% of NaPCP was mineralized in 15 min and nearly 100% of NaPCP was mineralized in 6 h by Bi_3O_4Br under visible light irradiation, confirming that Bi_3O_4Br is a superior visible light driven photocatalyst for complete decomposition of chlorinated phenol derivative (Fig. 9d).

To reveal the roles of the active oxygen species on the photodegradation NaPCP over Bi_3O_4Br , we utilized benzoquinone, KI, $K_2Cr_2O_7$, iso-propanol as $\bullet O_2^-$, hole, e^- , and $\bullet OH$ scavengers [32–34], respectively. The addition of benzoquinone could inhibit 90.4% of NaPCP degradation, while the inhibition efficiencies of KI and $K_2Cr_2O_7$ were about 89.6% and 71.6%, respectively (Fig. 10a). By contrast, the presence of iso-propanol could slightly inhibit the degradation of NaPCP to a degree of 6.5%. These active species trapping experimental results imply that $\bullet O_2^-$ is crucial for the photodegradation of NaPCP over Bi_3O_4Br . It is known that $\bullet O_2^-$ would react with H^+ to produce HO_2 and two HO_2 could further generate H_2O_2 and an oxygen molecule. The generated H_2O_2 could then capture an electron to produce $\bullet OH$. We therefore detected H_2O_2 generated during the Bi_3O_4Br photocatalysis and found that the concentration of H_2O_2 increased in the first 5 min and then decreased (Fig. 10b). This observation is consistent with the weak signals of DMPO- $\bullet OH$ appeared in the Bi_3O_4Br aqueous suspension (Fig. 6d).

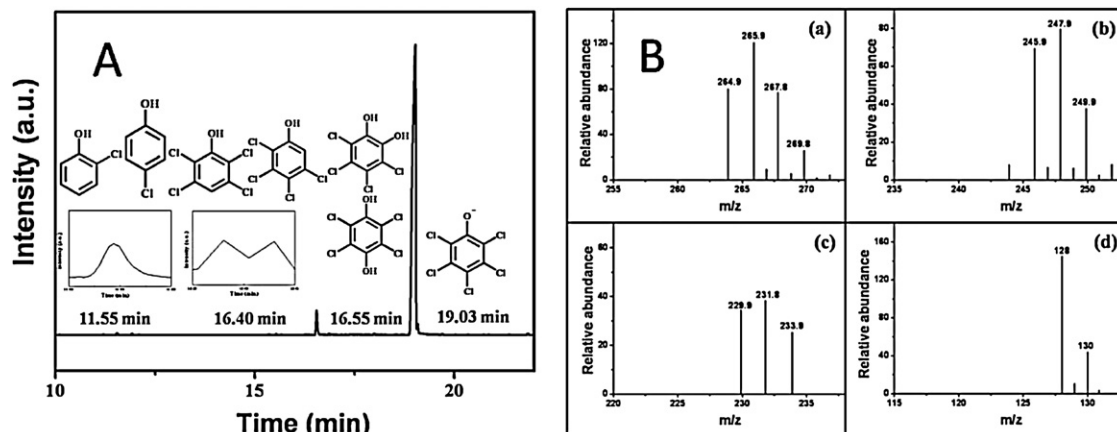


Fig. 11. The HPLC spectra (A) and mass spectra (B) of the intermediates during the photocatalytic degradation of NaPCP over Bi_3O_4Br . (a) The mass spectra of pentachlorophenol negative ion; (b) the mass spectra of 2,3,5,6-tetrachloro-1,4-pyrocatechol and 3,4,5,6-tetrachloro-1,2-pyrocatechol; (c) the mass spectra of 2,3,5,6-tetrachlorophenol and 2,3,4,5-tetrachlorophenol; (d) the mass spectra of parachlorophenol and o-chlorophenol.

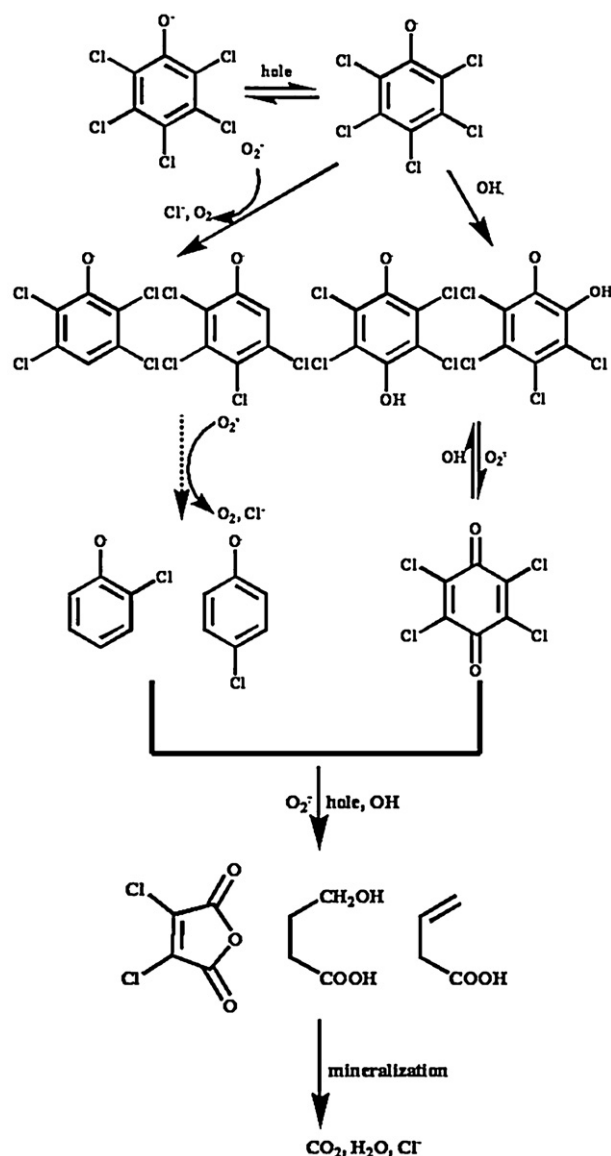
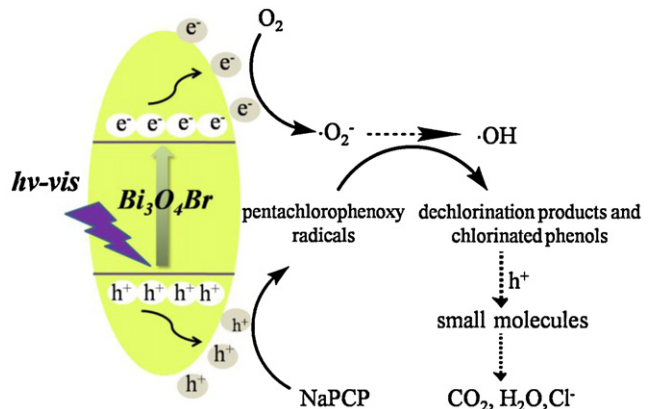


Fig. 12. The possible photocatalytic decomposition pathway of NaPCP.

GC-MS analysis was used to study the photocatalytic decomposition pathway of NaPCP over $\text{Bi}_3\text{O}_4\text{Br}$ under visible light. Fig. 11 shows the HPLC and mass spectra of the intermediates generated during the photocatalytic degradation of NaPCP



Scheme 1. Photocatalysis process and possible degradation pathway of sodium pentachlorophenate over $\text{Bi}_3\text{O}_4\text{Br}$ under visible light irradiation.

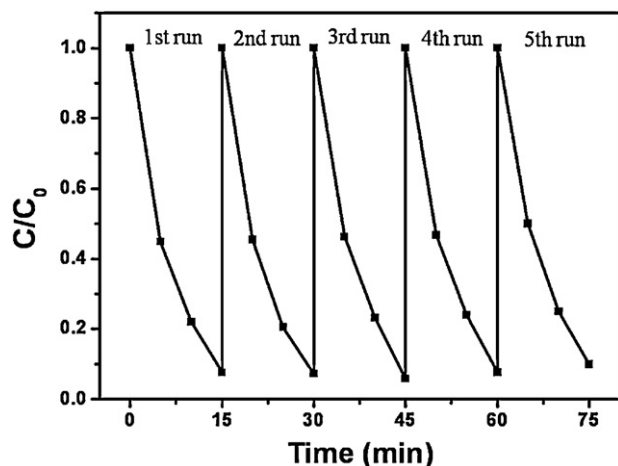


Fig. 13. Five cycles of photocatalytic degradation of NaPCP over $\text{Bi}_3\text{O}_4\text{Br}$ under visible light irradiation.

over $\text{Bi}_3\text{O}_4\text{Br}$, which reveals the existence of pentachlorophenol negative ion, 2,3,5,6-tetrachloro-1,4-pyrocatechol, 3,4,5,6-tetrachloro-1,2-pyrocatechol, 2,3,5,6-tetrachlorophenol, 2,3,4,5-tetrachlorophenol, parachlorophenol, and 1,2-dichlorophenol. On the basis of the intermediates and the above active species trapped experimental results, we proposed a possible photocatalytic decomposition pathway of NaPCP over $\text{Bi}_3\text{O}_4\text{Br}$ (Fig. 12). First, pentachlorophenol negative ion would be attacked by photo-generated holes to generate pentachlorophenoxy radicals, which

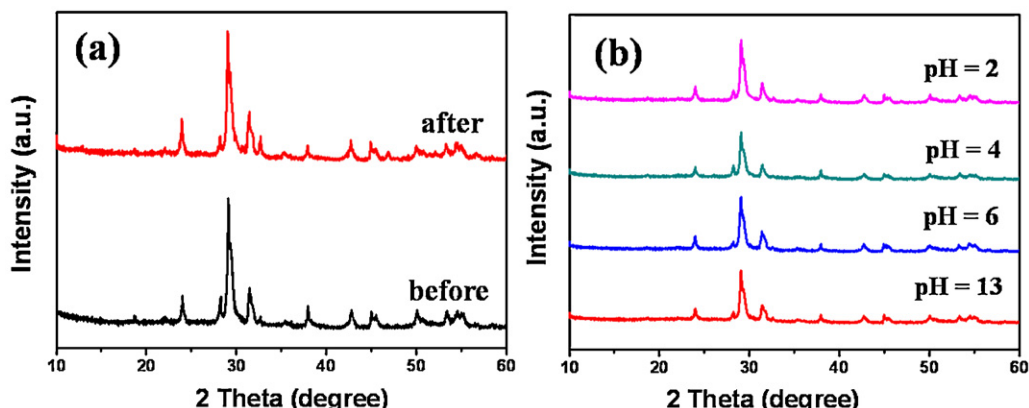


Fig. 14. (a) XRD patterns of $\text{Bi}_3\text{O}_4\text{Br}$ before and after photodegradation; (b) XRD patterns of $\text{Bi}_3\text{O}_4\text{Br}$ after being suspended aqueous solution with different pH values.

could easily be oxidized by active species. Considering the electron negativity and resonance effect of the radicals, the ortho- and para- positions are more easily attacked by negatively charged radicals, like electrons and $\bullet\text{O}_2^-$ [35]. So the photogenerated electrons and $\bullet\text{O}_2^-$ could directly attack the C–Cl bond on the benzene ring to initiate dechlorination process. Meanwhile, $\bullet\text{OH}$ radical was generated by multistep reduction $\bullet\text{O}_2^-$ in this system and could also assault the ortho- and para- position of NaPCP to generate 2,3,5,6-tetrachloro-1,4-pyrocatechol and 3,4,5,6-tetrachloro-1,2-pyrocatechol. As further attacked by photogenerated holes, these intermediates would be further oxidized to benzoquinone, followed with the destroying of double bonds in the benzene ring and the generation of small molecules compounds. However, we could not detect any small molecule compounds by GC–MS analysis, which could be attributed to the low concentration and instability of these intermediates in the solution. Finally, the small molecule compounds could be completely mineralized to CO_2 and H_2O , as revealed by TOC analysis. The photocatalysis processes of BiOBr and $\text{Bi}_3\text{O}_4\text{Br}$ as well as the possible degradation way of NaPCP over BiOBr and $\text{Bi}_3\text{O}_4\text{Br}$ are proposed in Scheme 1.

To evaluate the reusability and stability of the $\text{Bi}_3\text{O}_4\text{Br}$, the used catalyst was washed with deionized water and ethanol, and dried at 50 °C for the next cycle of photodegradation. The photocatalytic activity of $\text{Bi}_3\text{O}_4\text{Br}$ did not decline (Fig. 13) and its crystal structure did not change according to the XRD analysis (Fig. 14a) after five cycles of the photodegradation. Meanwhile, $\text{Bi}_3\text{O}_4\text{Br}$ was also stable in aqueous solution with pH values from 2 to 13 (Fig. 14b). Therefore, we conclude that $\text{Bi}_3\text{O}_4\text{Br}$ is a superior photocatalyst for environmental pollution control.

4. Conclusion

In summary, we have demonstrated $\text{Bi}_3\text{O}_4\text{Br}$ could exhibit much higher photocatalytic performance than BiOBr on the degradation of NaPCP under visible light ($\lambda \geq 420\text{ nm}$) irradiation. DFT calculations and experimental results revealed the conduction band of $\text{Bi}_3\text{O}_4\text{Br}$ became negatively with increasing Bi content and then could reduce molecular oxygen to produce $\bullet\text{O}_2^-$. The generation of $\bullet\text{O}_2^-$ could not only inhibit the recombination of photoinduced charge carriers, but also benefit the dechlorination of chlorinated phenol derivative. This study provides a new photocatalyst for chlorinated phenol derivative removal with solar light and some insight for the design of highly efficient visible light active photocatalysts.

Acknowledgements

This work was supported by National Basic Research Program of China (973 Program) (Grant 2013CB632402), National Science Foundation of China (Grants 21073069, 91023010, and 21177048).

References

- [1] K. Morimoto, K. Tatsumi, Chemosphere 34 (1997) 1277–1283.
- [2] J.W. Liu, R. Han, H.T. Wang, Y. Zhao, W.J. Lu, H.Y. Wu, T.F. Yu, Y.X. Zhang, Journal of Molecular Catalysis A: Chemical 344 (2011) 145–152.
- [3] M. Fukushima, K. Tatsumi, Environmental Science and Technology 35 (2001) 1771–1778.
- [4] T. Luo, Z.H. Ai, L.Z. Zhang, Journal of Physical Chemistry C 112 (2008) 8675–8681.
- [5] G.D. Karamanev, R. Samson, Environmental Science and Technology 32 (1998) 994–999.
- [6] X.F. Chang, J. Huang, Q.Y. Tan, M. Wang, G.B. Ji, S.B. Deng, G. Yu, Catalysis Communications 10 (2009) 1957–1961.
- [7] X.F. Chang, G.B. Ji, Q. Sui, J. Huang, G. Yu, Journal of Hazardous Materials 166 (2009) 728–733.
- [8] J.W. Liu, R. Han, Y. Zhao, H.T. Wang, W.J. Lu, T.F. Yu, Y.X. Zhang, Journal of Physical Chemistry C 115 (2011) 4507–4515.
- [9] X. Zhang, Z.H. Ai, F.L. Jia, L.Z. Zhang, Journal of Physical Chemistry C 112 (2008) 747–753.
- [10] H.J. Zhang, L. Liu, Z. Zhou, Physical Chemistry Chemical Physics 14 (2012) 1286–1292.
- [11] Z.T. Deng, D. Chen, B. Peng, F.Q. Tang, Crystal Growth and Design 8 (2012) 2995–3002.
- [12] Z.F. Jia, F.M. Wang, F. Xin, B.Q. Zhang, Industrial and Engineering Chemistry Research 50 (2011) 6688–6694.
- [13] J. Jiang, X. Zhang, P.B. Sun, L.Z. Zhang, Journal of Physical Chemistry C 115 (2011) 20555–20563.
- [14] Z.H. Ai, W.K. Ho, S.C. Lee, L.Z. Zhang, Environmental Science and Technology 43 (2009) 4143–4150.
- [15] Z.H. Ai, W.K. Ho, S.C. Lee, Journal of Physical Chemistry C 115 (2011) 25330–25337.
- [16] J. Zhang, F.J. Shi, J. Lin, D.F. Chen, J.M. Gao, Z.X. Huang, X.X. Ding, C.C. Tang, Chemistry of Materials 20 (2008) 2937–2941.
- [17] A. Walsh, Y.F. Yan, M.N. Huda, M.M. Al-Jassim, S.H. Wei, Chemistry of Materials 21 (2009) 547–551.
- [18] H.B. Hu, C.S. Pan, W.Q. Yao, Y.F. Zhu, Journal of Physical Chemistry B 109 (2005) 22432–22439.
- [19] A.L. Lamus, G.L. Kok, S.N. Gitlin, J.A. Lind, Analytical Chemistry 57 (1985) 917–922.
- [20] J. Ryu, W. Choi, Environmental Science and Technology 40 (2006) 7034–7039.
- [21] J. Ryu, W. Choi, Environmental Science and Technology 38 (2004) 2928–2933.
- [22] J. Cao, B.Y. Xu, B.D. Luo, H.L. Lin, S.F. Chen, Catalysis Communications 13 (2011) 63–68.
- [23] S. Shenawi-Khalil, V. Uvarov, Y.L. Kritsman, E. Menes, I. Popov, Y. Sasson, Catalysis Communications 12 (2011) 1136–1141.
- [24] Y. Li, J.F. Niu, L.F. Yin, W.L. Wang, Y.P. Bao, J. Chen, Y.P. Duan, Journal of Environmental Science 11 (2011) 1911–1918.
- [25] W. Wei, Y. Dai, B.B. Huang, Journal of Physical Chemistry C 113 (2009) 5658–5663.
- [26] J.W. Wang, Y.D. Li, Chemical Communications 18 (2003) 2320–2321.
- [27] H. Deng, J.W. Wang, Q. Peng, X. Wang, Y.D. Li, Chemistry- A European Journal 11 (2005) 6519–6524.
- [28] Y.N. Wang, K.J. Deng, L.Z. Zhang, Journal of Physical Chemistry C 115 (2011) 14300–14308.
- [29] A. Ishikawa, T. Takata, J.N. Kondo, M. Kara, H. Kobayashi, K. Domen, Journal of the American Chemical Society 124 (2002) 13547–13553.
- [30] J.S. Zhang, X.F. Chen, K. Takanabe, K. Maeda, K. Domen, J.D. Epping, X.Z. Fu, M. Antonietti, X.C. Wang, Angewandte Chemie 122 (2010) 451–454.
- [31] V.Y. Svetlana, M.R. Kevin, Science 320 (2008) 218–222.
- [32] S.X. Ge, L.Z. Zhang, Environmental Science and Technology 45 (2011) 3027–3033.
- [33] M.C. Yin, Z.S. Li, J.H. Kou, Z.G. Zou, Environmental Science and Technology 43 (2009) 8361–8366.
- [34] Y.M. Chen, A.H. Lu, Y. Li, L.S. Zhang, H.Y. Yip, H.J. Zhao, T.C. An, P.K. Wong, Environmental Science and Technology 45 (2011) 5689–5695.
- [35] Q. Lan, F.B. Li, C.S. Liu, X.Z. Li, Environmental Science and Technology 42 (2008) 7918–7923.